Nuclear Science and Techniques (2026) 37:110
https://doi.org/10.1007/s41365-026-01927-0

# A low-background beta detection system using a time projection chamber

Rui-Yang Zhang[1,2] · Zhi-Yong Zhang[1,2] · Zeng-Xuan Huang[1,2] · Yong Zhou[1,2] · Jian-Bei Liu[1,2] · Song-Song Tang[1,3] · Yuan-Fei Cheng[1,2] · Chang-Qing Feng[1,2] · Ming Shao[1,2] · Yi Zhou[1,2]

Received: 6 January 2025 / Revised: 24 March 2025 / Accepted: 25 March 2025 / Published online: 28 March 2026


## Abstract
In this study, we present a time projection chamber (TPC) system for low-background beta radiation measurements. The system consists of a TPC with a two-dimensional strip readout Micromegas and an anti-coincidence detector with readout pads for cosmic ray vetoing. The detector system uses an AGET-based waveform sampling system for data acquisition. The beta detection capability of the system was verified through an experimental test using $^{90}$Sr beta source. In addition, a dedicated simulation program based on Geant4 was developed to model the entire detection process, including the responses to both the beta source and background radiation. The simulation results were compared with the experimental data for both beta and background samples, and they were in good agreement. Simulation samples were used to optimize and train the classification models for beta and background discrimination. By applying the selected model into test data, the system achieved a background rate of 0.49 cpm/cm$^2$ while retaining more than 55% of $^{90}$Sr beta signals within a 7 cm diameter detection region. Further analysis revealed that approximately 70% of the background originated from environmental gamma radiation, while the remaining contribution mainly originated from the intrinsic radioactivity of the detector materials, particularly the FR-4-based field cage and readout plane. Based on the knowledge gained from the experiments and simulations, an optimization of the TPC system was proposed, with the simulation predicting a potential reduction in the background rate to 0.0012 cpm/cm$^2$.

**Keywords** Gaseous detector · Time projection chamber · Micromegas · Low-background beta detection · Detector modeling and simulations · Data processing methods

## 1 Introduction

Since the discovery of alpha and beta radiation by Rutherford in 1899 [1], their properties have been extensively studied and utilized in nuclear physics experiments. Alpha and beta radiation are commonly found in the environment and generally originate from natural and human-produced radionuclides [2]. In specific situations, it is crucial to monitor radiation levels to ensure that they remain within safety standards [3]. For instance, measurements of $^{90}$Sr radioactivity in environmental samples near the Fukushima Daiichi Nuclear Power Plant in 2013 provided insights into nuclide mitigation following the nuclear accident [4]. Similarly, the radioactivity of alpha- and beta-emitting sources was monitored at the Qinshan Nuclear Power Plant for a long period of time [5, 6]. In rare-event search experiments, alpha and beta radiation from uranium and thorium decay chains can

This work was supported by the National Natural Science Foundation of China (No. 12125505), and the State Key Laboratory of Particle Detection and Electronics (No. SKLPDE-ZZ-202401).

✉ Zhi-Yong Zhang
zhzhy@ustc.edu.cn

1 State Key Laboratory of Particle Detection and Electronics, University of Science and Technology of China, Hefei 230026, China

2 Department of Modern Physics, University of Science and Technology of China, Hefei 230026, China

3 School of Nuclear Science and Technology, University of Science and Technology of China, Hefei 230026, China

significantly contribute to background signals [7]. Evaluating and suppressing these backgrounds is critical for achieving the desired sensitivity, as demonstrated in experiments such as XENON [8], NEXT [9], and NνDEx [10]. Beyond nuclear and high-energy physics, alpha and beta radiation detection is essential for monitoring pollution in drinking water and food [11–15]. In all these scenarios, accurately determining the radiation level is vital.

However, radiation signals from samples are often accompanied by natural background radiation, necessitating the development of low-background detection techniques for precise measurements. The primary sources of background radiation include environmental gamma rays, cosmic rays, and radioactive contamination in construction materials, with their contributions varying depending on the detection technique and type of radiation being measured [16, 17]. Although several solutions exist for pursuing low-background radiation measurements [18], including commercially available detectors based on proportional counters or scintillators [19–22], these techniques rely primarily on counting rates and pulse height information to distinguish between different radiation types. This approach imposes limitations, particularly in beta radiation detection, because its energy loss is similar to that of environmental background radiation. Consequently, these detectors lack the ability to actively separate beta signals from background noise, often requiring thick lead shielding layers (typically 10 cm) to achieve low background rates. Such shielding materials restrict the detection volume and compromise system portability.

To address these limitations, we propose the use of a time projection chamber (TPC) as the foundational concept for low-background alpha and beta radiation detection [23]. It can simultaneously measure the 3D track and energy deposition of charged particles within the detector. By leveraging the detailed information provided by the incoming particles, it is possible to effectively discriminate the target particles of interest from the background noise. Furthermore, compared with traditional proportional counter-based techniques, TPC provides the additional advantage of event localization, enabling the determination of the spatial distribution of radiation in the sample.

In our previous study [23], a micromegas-based time projection chamber (TPC) prototype was developed for low-background alpha detection. The results demonstrated an alpha background rate of less than $1.6\times10^{-3}$ cpm at a 95% confidence level without shielding, while achieving a $^{241}$Am acceptance rate of 96%. The excellent performance in alpha particle detection highlights the potential of TPC technology for low-background radiation detection [24, 25]. Building on this success, we developed a new TPC system for low-background beta radiation detection. Unlike alpha particles, beta particles have significantly weaker ionization powers, resulting in longer track lengths [26]. Furthermore, beta detection is subject to additional background sources, such as cosmic rays and environmental gamma radiation. To address these challenges, we optimized the TPC system design to improve its sensitivity and discrimination capabilities. A dedicated simulation program was established to model the detector response, providing insights into its performance and the separation of beta signals from background events.

In this paper, we present the design, fabrication, simulation, and test results of the TPC prototype for beta radiation detection in Sects. 2–5. The origins of the beta detection background are investigated in Sect. 6 using both experimental data and simulation data. Finally, further optimizations of the detector are discussed in Sect. 7, with simulations predicting an anticipated reduction in the background radiation rate.

## 2 Detector structure

The new TPC prototype builds upon the experience gained from the previous version and is optimized to achieve a larger detection area while effectively suppressing the background for beta radiation detection. The system consists of two subdetectors assembled back-to-back: a TPC detector and an anti-coincidence detector, as shown in Fig. 1. The TPC detector serves as the primary detection element for beta particles, whereas an anti-coincidence detector is employed to veto the cosmic ray background. The drift lengths of the TPC detector and the anti-coincidence detector are 55 mm and 8 mm, respectively. For clarity, the term “TPC” will refer to the TPC detector alone, while “TPC system” will refer to the entire combined detection system hereafter.

Thermal-bonded Micromegas [27, 28] is used as both the readout plane of the TPC and the anti-coincidence detector. The core component of the Micromegas is a stainless-steel mesh bonded to a printed circuit board (PCB) with a thermal bonding adhesive, forming a 100 mm amplification gap. The readout electrodes of the two detectors were located on opposite sides of the PCB. The PCB is a 10-layer board with a thickness of 2.3 mm, sufficient to block beta particles with energies below 5 MeV from reaching the anti-coincidence detector. To provide discharge protection, a germanium layer with a sheet resistivity of approximately 100 MΩ/sq is coated on top of the readout electrodes [29]. The readout electrode structures differed between the two subdetectors. For the TPC detector, the signals were read using two sets of orthogonally arranged strips. These two-dimensional strips are positioned on the same layer of the PCB and collectively cover the entire detection plane (Fig. 2 (a)).

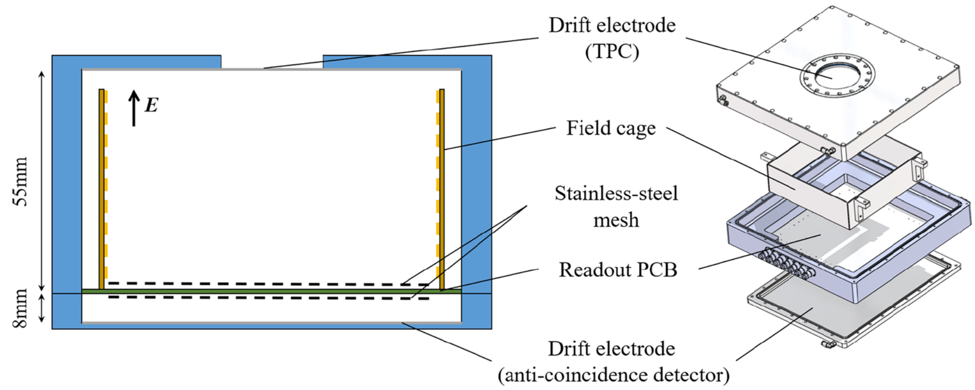


**Fig. 1** (Color online) Schematic layout (left) and the mechanical drawing (right) of the TPC system

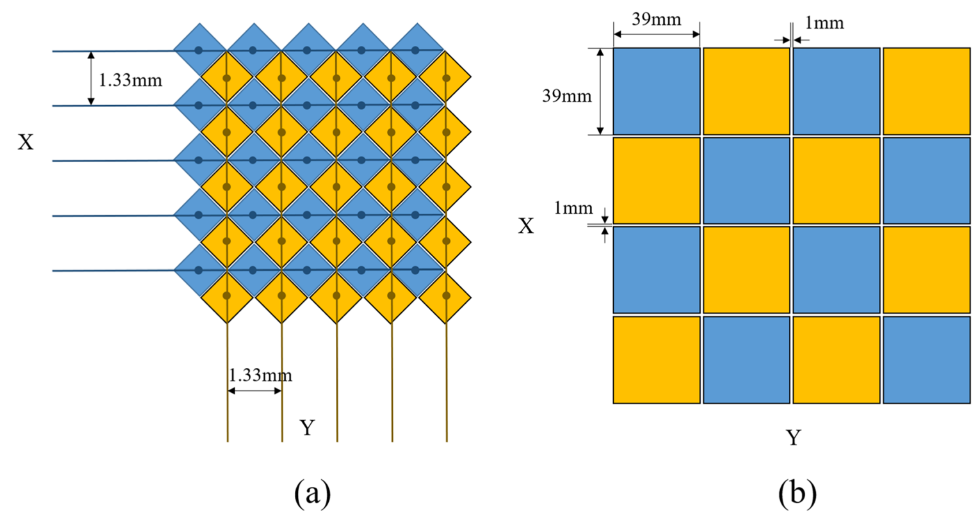


**Fig. 2** (Color online) Arrangement of the TPC's readout strips (a) and the anti-coincidence detector's readout pads (b)

Each strip in the TPC readout has a width of 1.33 mm, with 120 strips per dimension, resulting in a total sensitive area of $160\,\mathrm{mm} \times 160\,\mathrm{mm}$. This design ensured that the weighting field experienced by the two-dimensional strips was identical, thereby producing uniform responses across both dimensions. The spatial resolution of the TPC was measured using a collimated $^{241}$Am source, yielding a consistent result of approximately 0.6 mm in both the X and Y directions. In contrast, the anti-coincidence detector, primarily used to veto cosmic ray events, adopts coarser segmentation to minimize the number of required electronic channels. Its $160\,\mathrm{mm} \times 160\,\mathrm{mm}$ sensitive area is divided into a $4 \times 4$ grid of square pads, with each pad being read out independently. Each pad is $39\,\mathrm{mm} \times 39\,\mathrm{mm}$ in size, with a 1 mm gap between adjacent pads, shown in Fig. 2 (b). The TPC features a circular incident window with a diameter of 7 cm. This window was constructed using a 2.7 µm thick PET film coated with aluminum, designed to minimize energy loss as particles traverse it. The film was electrically grounded by connecting it to the aluminum shell of the detector, which also served as part of the drift electrode plane.

For the TPC, the design of the field cage is critical to ensure a uniform electric field within the sensitive volume. Nonuniformities in the electric field can cause abrupt changes in the electron drift velocity, thereby affecting the track reconstruction accuracy and complicating event discrimination. While this issue is less significant for alpha detection because alpha particle tracks are short and primarily confined to the central region, where field distortion is minimal, it becomes more prominent for beta detection. Beta particles, even with energies of a few tens of kiloelectronvolts, have a higher probability of traversing the entire TPC, thereby making the field uniformity essential. To address this, a staggered double-layer strip arrangement was adopted for the field cage [30]. The field cage comprised four PCBs that enclosed a sensitive volume. On both the inner and outer surfaces of each PCB, 3.6 mm wide copper strips were arranged with a pitch of 4 mm, with the inner and outer strips displaced by half a pitch. Adjacent strips are connected via resistors to create a uniform voltage gradient when a voltage is applied to the bottom strip of the sensor. The double-layer design provided a key benefit by mitigating the edge effects by shielding the external ground voltages.

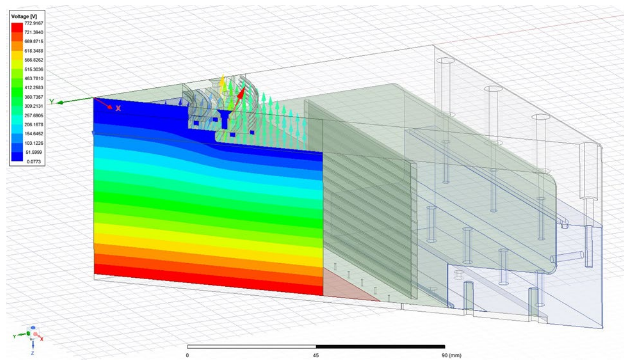

**Fig. 3** (Color online) Simulated voltage distribution within the central 120 mm × 120 mm region of the TPC. These voltages correspond to the typical settings used for beta radiation detection. Due to the symmetry of the design, only one-eighth of the TPC is modeled

An electromagnetic simulation using ANSYS Maxwell confirmed that, after optimization, the voltage distribution was smooth and uniform across the entire sensitive volume (Fig. 3).

## 3 Experimental setup

The TPC system was filled with a gas mixture of 96.5% argon and 3.5% isobutane during all tests. The drift cathode was mechanically connected to the detector shell, which automatically set it to the ground level. The amplification voltage was fixed to 390 V after optimization for the desired avalanche gain. The stainless-steel mesh and resistive anode layer were biased at specific positive voltages to maintain an appropriate drift field and a high electron collection efficiency. The anode strips (or pads) of the TPC system were connected to an electronic system for data acquisition and processing. The electronic system used in this experiment was an AGET chip [31] based multichannel waveform sampling system developed at USTC [32]. Signals from the anode channels of both the TPC and anti-coincidence detector were first sent to a front-end card (FEC), where they were amplified, shaped, sampled, and digitized. The shaping time of the FEC was set to 500 ns. For each channel, the signal waveform was digitized at a sampling rate of 25 MHz with 512 sampling points, resulting in a time window of 20 µs. This time window was chosen to cover the maximum drift time of an ionization track generated by beta particles in the TPC, which is approximately 2 µs. The digitized waveform data were then transmitted to a data collection module (DCM), which aggregated the information from the FEC and organized the signals from different channels into distinct events. Finally, these event packets were sent to a personal computer for further analysis. A photograph of the TPC system and its associated electronics are shown in Fig. 4.

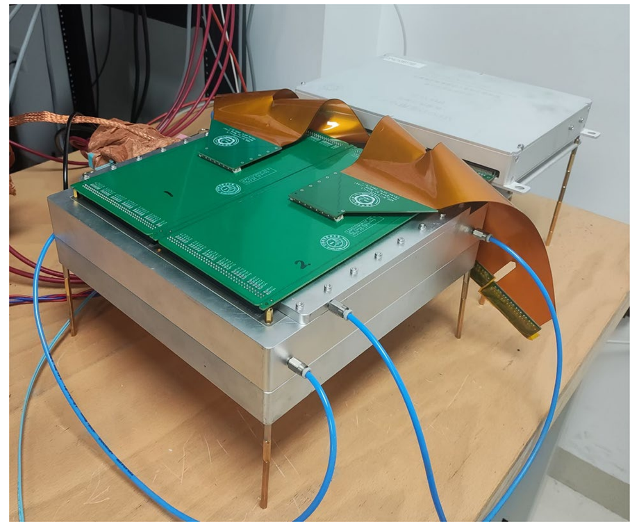

**Fig. 4** (Color online) A photograph of the TPC system during beta background test

In this study, a $^{90}$Sr surface beta source with a diameter of 1 cm was used to generate reference beta radiation events. The source was placed at the center of the incident window, 5 cm away from the window, during the tests. The decay product of $^{90}$Sr is $^{90}$Y, which undergoes beta decay. The recorded events included beta particles from both $^{90}$Sr and $^{90}$Y, with decay energies of 0.546 MeV and 2.28 MeV, respectively [33]. In addition to the beta source data, background data were collected under the same test conditions (voltages and working gas) but without the beta source to assess the background performance of the detector system.

As mentioned earlier, the test data were stored as event packages. Each event package contains the numbers of all hit channel signal waveforms, from which we can reconstruct the energy deposition and particle tracks. The amplitude of each waveform is proportional to the charge collected by the channel and thus is proportional to the energy deposited in the region corresponding to that detector channel. Therefore, the sum of the amplitudes of all channels represents the total energy deposition in the TPC for a given particle. The position of an ionization can be determined using the hit channel position and signal arrival time. Because the TPC uses a two-dimensional strip readout structure, it allows for 2D track reconstruction in the XZ and YZ planes.

Figure 5 (top row) shows a typical reconstructed beta particle track projected onto the XZ and YZ planes, where the particle scattering owing to multiple interactions is illustrated. The Z-dimensional drift length is determined by the arrival time measured using the 20% constant fraction timing method on the corresponding strip. The amplitude of each channel, which represents the energy deposition, is also shown for reference.

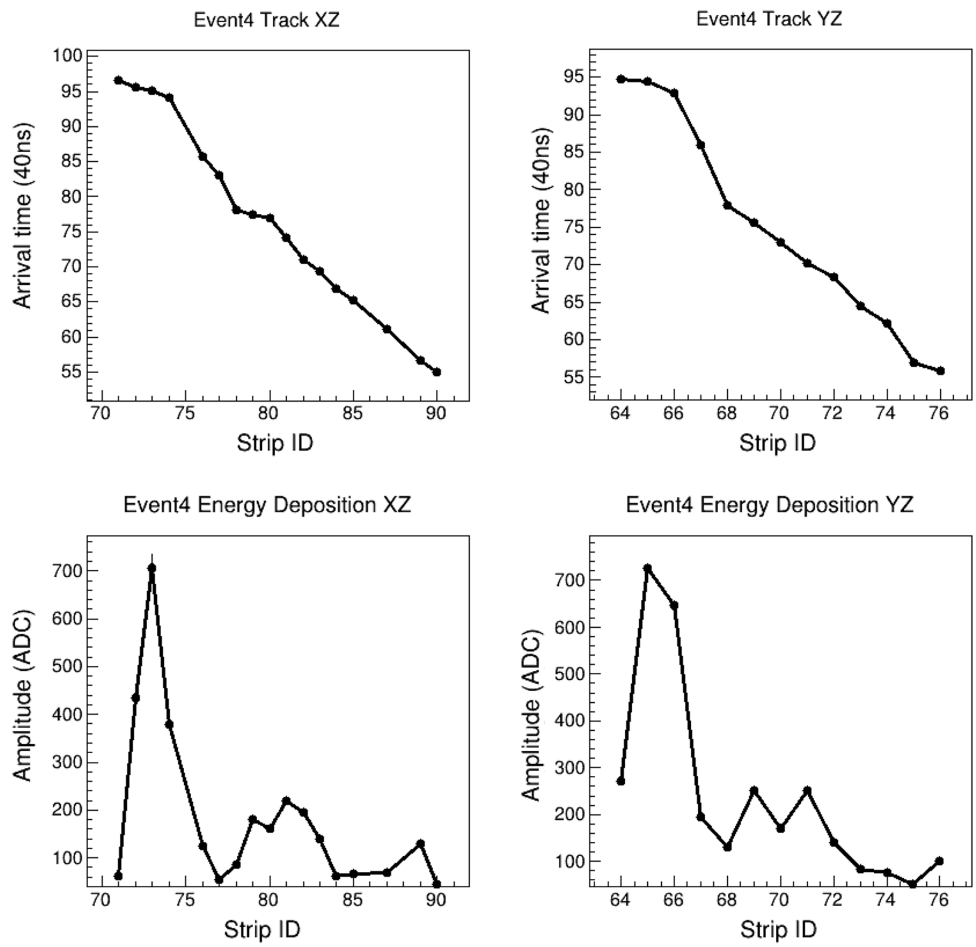


**Fig. 5** A beta event detected by the TPC. Top row: 2D projected tracks on XZ and YZ planes. The Z-dimension of the track is denoted by the signal arrival time of each strip. Bottom row: waveform amplitudes on X and Y strips

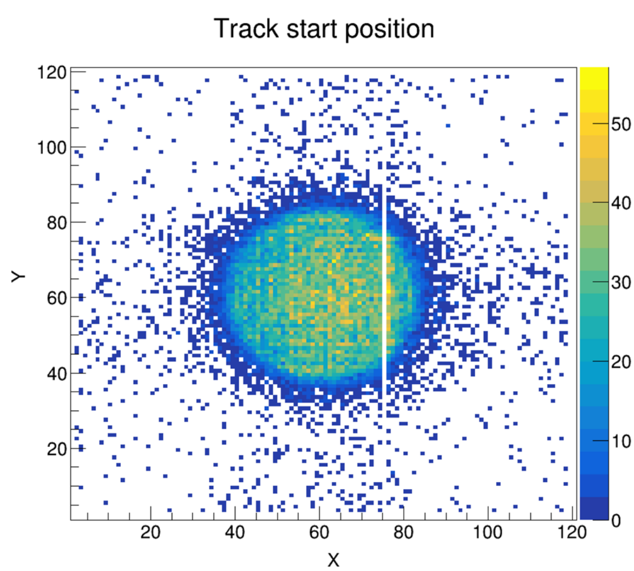


**Fig. 6** (Color online) Start position map of $^{90}$Sr beta test data

The starting position map of the beta particles is illustrated in Fig. 6. The start position is defined by combining the X and Y strip numbers with the longest drift time for each event, which corresponds to the position where the particle first enters the TPC volume. The reconstructed starting positions for the beta particles were primarily concentrated in a central circular area, the size of which was consistent with that of the detector entrance window. This is understandable because beta particles are easily blocked by the detector frame outside the entrance region. A missing channel in the X-dimension is attributed to its connection to a noisy channel on the AGET chip, such that the output signal from this channel is dropped. These test results indicate that the TPC system is capable of detecting beta particles and recording their 3D trajectories.

## 4 Detector simulation

As discussed in the previous section, we obtained test data for the $^{90}$Sr beta source and background events. To further distinguish beta source events from background events, it is essential to gain a deeper understanding of different behaviors exhibited by these events. For this purpose, a Monte Carlo simulation based on the Geant4 software [34] was conducted to model the signal generation process for both radioactive beta sources and background particles.

The detector geometry used in the simulation was constructed according to the mechanical design of the TPC system, with some simplifications in the detailed structure. A central region of 160 mm × 160 mm was defined as the sensitive area. The drift gaps for the TPC and the anti-coincidence detector were 55 mm and 8 mm, respectively. A filter was applied to select electrons generated by physical processes other than ionization, ensuring that only the primary electron tracks were counted. These include beta particles from beta decay and electrons produced by photon interactions with materials.

The aforementioned part of the simulation can be implemented using Geant4. However, the simulation results could not be directly compared with our test data because the simulation did not account for the detector and electronics response. To bridge this gap, an additional digitization process was incorporated into the simulation program, which converted the Monte Carlo truth information into waveforms on the electronic channels.

For a given simulated electron track, the ionized electrons along the track were grouped and drifted toward the anode plane under an electric field. The drift parameters for our working gas mixture (96.5% Ar + 3.5% $iC_4H_{10}$) were derived from Garfield++ simulations [35]. Under our test conditions for beta particles and their background, the drift field was set to approximately 120 V cm$^{-1}$, where the electron drift velocity is 3.72 cm s$^{-1}$, and the longitudinal and transverse diffusion coefficients are 0.037 cm$^{1/2}$ and 0.055 cm$^{1/2}$, respectively. The arrival position and time of each drifted electron cluster were calculated by assuming a constant drift velocity with a random Gaussian-distributed displacement both horizontally and vertically, based on the diffusion coefficients.

The drifted electrons induced charge signals on the anode plane following the avalanche process in the micromegas, which was represented by a constant gain factor. The anode plane of the TPC was divided into X and Y strips, as illustrated in Fig. 2. To account for the effect of signal spreading on the resistive layer, a charge cluster induced a signal on its hit strip and on two adjacent strips in both X and Y dimensions. The total drifted charge was shared among these five strips, with the charge distribution on each strip being inversely proportional to its distance from the hit position. The collected charges on each strip were then convoluted with a given transfer function calibrated for the electronics to obtain an analog output signal. Finally, this signal was sampled at a rate of 25 MHz, producing the actual output signal waveform with 512 sampling points. This digitization process generated simulation data with the same format as the test data, enabling a direct comparison between the simulation results and test data, and allowing further optimization of the detector design based on the simulation outcomes.

Figure 7 shows a comparison between the MC truth and the reconstructed track after digitization and data processing. There was almost no difference in the track shape, indicating that the digitization process did not significantly affect the TPC tracking performance. Additionally, because digitization reflects the actual detector response, this result further implies that the designed detector readout segmentation is appropriate and that the multi-scattering effect does not significantly deteriorate track reconstruction.

To evaluate the reliability of our simulation and digitization program, the simulation results of the $^{90}$Sr beta source data were compared with test data. In the simulation, the beta source was positioned 5 cm away from the TPC entrance window, consistent with the test setup. A total of 80 million $^{90}$Sr decays and cascaded $^{90}$Y decays were simulated. Because the exact amplification gain in our test setup was unknown, a gain correction factor was introduced in the simulation to calibrate the energy spectrum peak position based on the test data. Figure 8 shows a comparison between the energy spectrum, X-dimensional hit channels, Y-dimensional hit channels, and total hit channels from the simulation and test data. The distributions were normalized to probability density functions for comparison purposes. The simulation results matched the test data well, with only one calibration parameter. The distortion observed in the test energy spectrum, compared with that in the simulation, is likely due to the inhomogeneous signal response across different regions of the readout plane. This effect leads to larger fluctuations in the induced charge signal. The main cause of this inhomogeneity is the nonuniformity of the avalanche gain. A previous test of the TPC showed that the nonuniformity was approximately 12.8% within the central region of the detector.

In addition to beta source events, obtaining information about background events through simulations is valuable. As the exact origin of the background is unknown, a reasonable assumption is that the majority of the background is caused by environmental gamma-induced electrons, given that cosmic ray muons have already been rejected by the anti-coincidence detector. Based on this assumption, we measured the gamma spectrum using a CZT detector and applied an unfolding algorithm [36] to obtain the true gamma flux in our laboratory. This gamma flux spectrum was then used as an input for our simulation program to generate the background data. Figure 9 shows a comparison between the simulated and tested backgrounds. Slight discrepancies were observed in the distribution of hit channel numbers between the test results and simulation, with the test data indicating a higher frequency of events with greater hit multiplicity. This implies that additional background sources, aside from

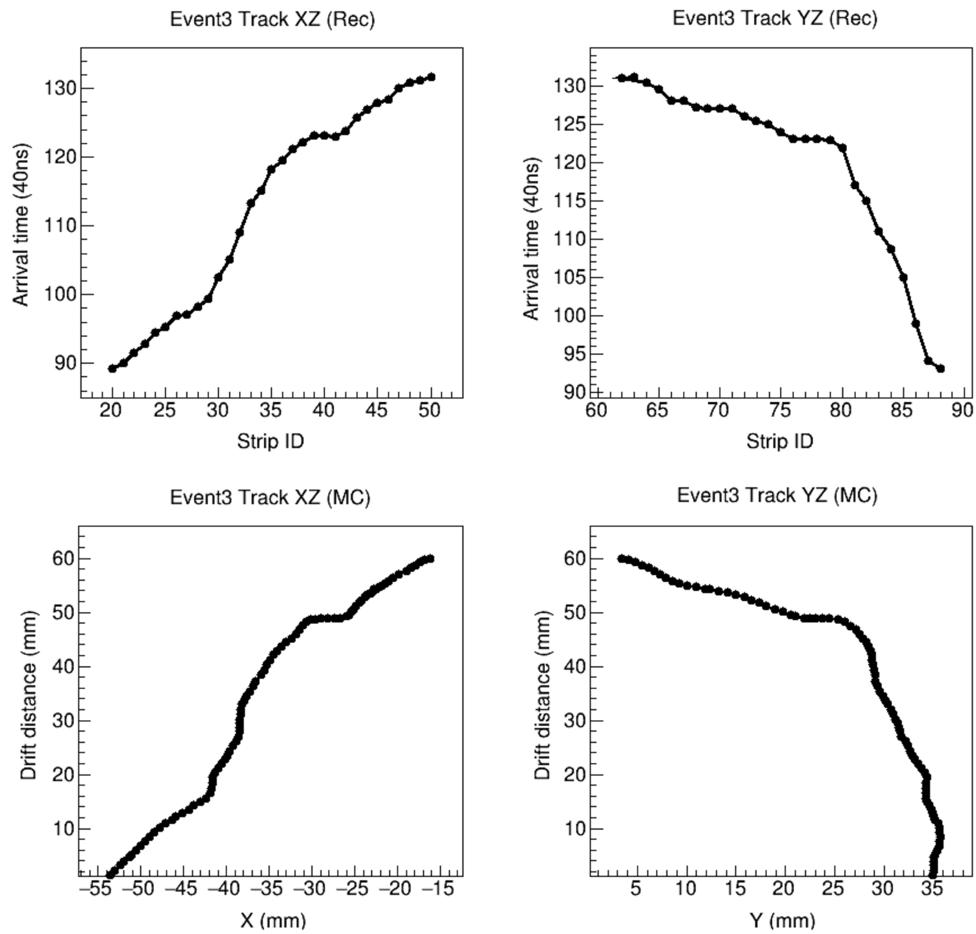


**Fig. 7** Comparison between reconstructed track (top) and MC truth track (bottom)

environmental gamma radiation, may be present under the experimental conditions, contributing to longer track lengths in the TPC. Nevertheless, the environmental gamma-induced background is believed to be the primary source. Further experimental tests and analyses, as discussed in Sect. 6, reinforce this conclusion and offer insights into the origins of the remaining background radiation sources. Also, the effect of these differences has turned out to be minor on beta background discrimination, which will be clarified in Sect. 5.

## 5 Beta and background discrimination

Discriminating between two types of data (beta signals and background in our case) is a classification problem [37]. Numerous algorithms have been developed for such problems, collectively known as multivariable analysis (MVA) methods, many of which are implemented in the ROOT TMVA toolkit [38]. In this study, several TMVA methods were tested to identify the best-performing algorithms. The variables used for classification included the deposited energy within the TPC, hit strip numbers in the X and Y dimensions, traversal time of a track inside the TPC, and reconstructed starting position on the XY plane.

Simulated beta and background datasets were used to test various algorithms, as we have already confirmed the consistency between the simulation and test data. A set of initial cuts was applied to both the beta signal and background events for preliminary selection. The following cuts were applied:

- The signal amplitude must be at least ten times the noise root mean square (RMS) above the baseline. This cut helps remove small signals generated by random noise without affecting the actual data.
- At least one hit strip in both the X and Y dimensions is required to enable track reconstruction in both the XZ and YZ planes. The results showed that nearly all events satisfied this criterion.
- The event should contain hits only within the TPC detector. Events with hits on the anti-coincidence detector were considered as background and discarded.
- The reconstructed start position of the event should be within the central window region. This crucial cut helps reduce the background from peripheral products while

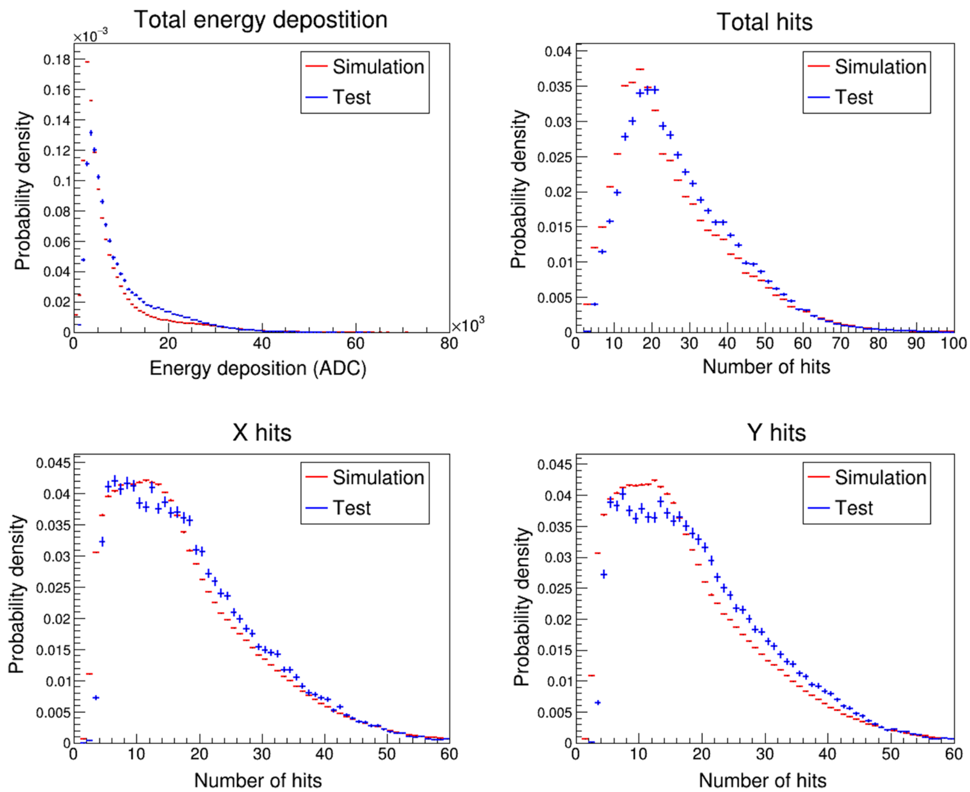


**Fig. 8** (Color online) Comparison of the distributions between simulation and test data for the $^{90}$Sr beta source

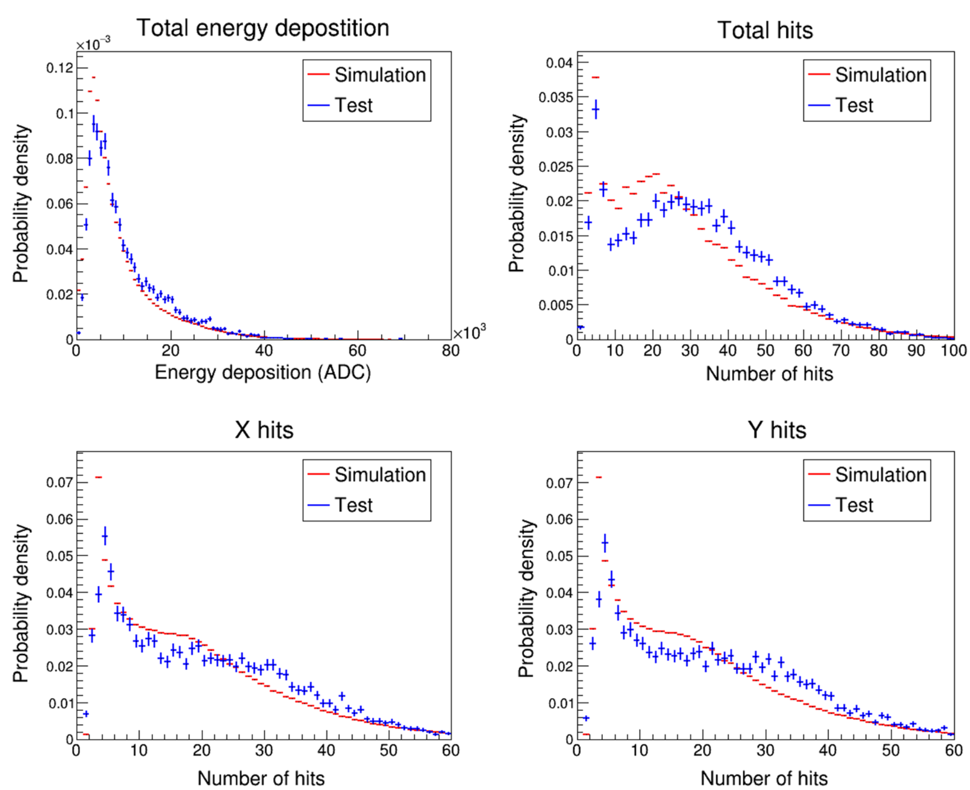


**Fig. 9** (Color online) Comparison of the distributions between simulation and test data for the background. The simulation data includes only gamma-induced background

preserving beta detection efficiency. Only a small fraction of beta particles are rejected by this cut owing to position reconstruction failure or multi-scattering effects.

A fiducial area with a diameter of 7 cm was defined using the above cuts. These cuts retained 95.5% of the original beta events while eliminating 81.9% of the background events. Using the remaining data samples, several commonly used MVA algorithms were trained and evaluated. The receiver operating characteristic (ROC) curves are shown in Fig. 10. The results demonstrate that the TMVA Boost Decision Tree (BDT) method achieved the best classification performance, even without parameter tuning. This is likely because the BDT method is particularly effective in handling variables with internal correlations.

Consequently, the TMVA BDT algorithm was selected as the most suitable discrimination method and used in the subsequent analysis.

The parameters of the BDT method were carefully tuned to maximize the discrimination performance. For instance, the training sample size was varied from 100,000 to 1 million to study its impact on the classification ability, as shown in Fig. 11. The background efficiency at a 55% signal efficiency was used as a metric to evaluate the discrimination quality. As the sample size increased, the discrimination performance initially improved but gradually reached a plateau. To balance the processing time and classification accuracy, a sample size of 200,000 was selected.

The trained BDT method was subsequently applied to analyze the actual test data. A $^{90}$Sr dataset with a 2 min acquisition time and a background dataset with a 60 min acquisition time were used as the signal and background samples, respectively. Because the background count rate is only approximately 0.6% of the $^{90}$Sr event rate, the $^{90}$Sr dataset is considered a pure signal sample. A classifier cutoff value was chosen to retain a 55% signal efficiency. Under these conditions, the corresponding background rejection rate was 86.3%, resulting in a background count rate of 18.8 counts per minute (cpm) within the sensitive area after discrimination, which is equivalent to 0.49 cpm/cm$^2$. The resulting BDT classifier distribution, along with the applied cutoff value, is shown in Fig. 12. Notably, when the trained BDT model was applied to the simulated beta and background datasets, the background rejection rate was 85.7% at the same signal efficiency. This result closely matches that obtained with the real data, indicating that the slight

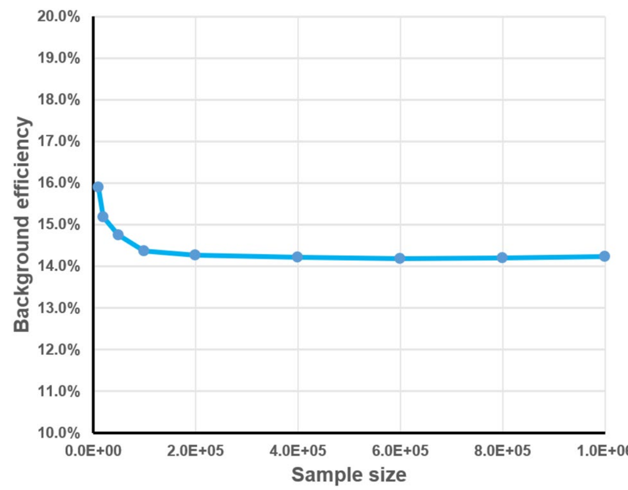


**Fig. 11** Training performance for TMVA BDT algorithm under different sample sizes

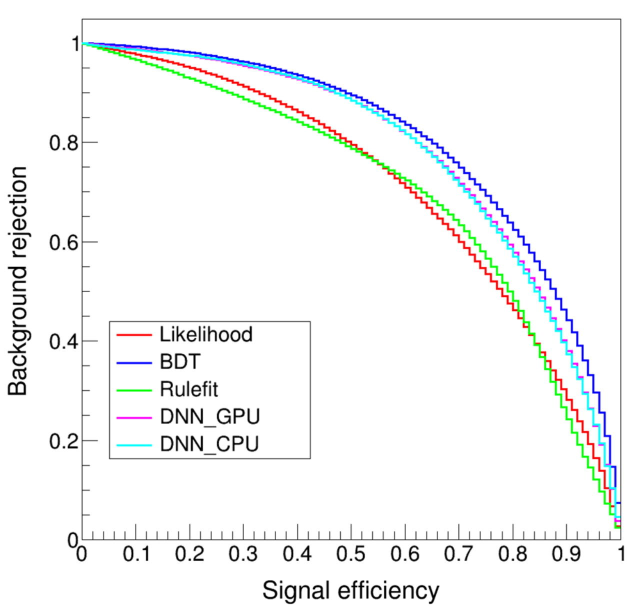


**Fig. 10** (Color online) ROC curves for different classification methods

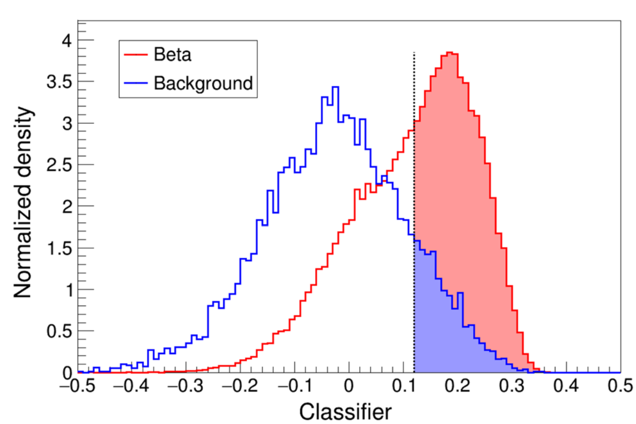


**Fig. 12** (Color online) Distribution of classifier values for the experimental beta and background samples. The dashed line marks the applied cut value

differences between the simulation and test data are tolerable for the algorithm, and a comparable discrimination performance can be achieved.

## 6 Background study

To further reduce the background rate to less than 0.1 cpm/cm$^2$ a detailed understanding of the origin of beta background is crucial. As mentioned in Sect. 4, we assumed that the primary source of the background in our TPC system was environmental gamma radiation, as cosmic ray-induced penetrating background events could be rejected by the anti-coincidence detector. Our top priority is to validate this hypothesis in future studies. Environmental gamma radiation primarily originates from gamma-emitting isotopes present in building materials and the atmosphere, typically with energies below 5 MeV. Such radiation can be effectively blocked using thick, high-$Z$ materials, which is a principle commonly applied in commercial beta detection devices to suppress the background. In simulations, we observed that adding a 5 cm-thick lead shell around the TPC system reduces the total gamma-induced background to approximately $7.3 \times 10^{-4}$ cpm/cm$^2$, which is less than 0.01% of the current value. This result demonstrates that a lead shield of this thickness is sufficient to block nearly all environmental gamma radiation exposure. We subsequently wrapped the TPC system with 5 cm-thick lead bricks to measure the remaining background radiation originating from other sources (Fig. 13).

Because the lead bricks used here are not radio pure and may contain beta-emitting isotopes, an additional 1 cm oxide-free copper board was placed between the lead and the TPC system to prevent beta particles from the lead radioisotopes from entering the TPC. The test results after shielding show that the background count rate was reduced to 30% of its original value, reaching approximately 1.04 cpm/cm$^2$ (without classification). This finding confirms that environmental gamma radiation is the primary source of the background radiation, which aligns with our previous assumption based on the simulation results.

The source of the remaining 30% of the background was further investigated. Because these background events were not blocked by the lead shielding, they must have originated from the materials of the TPC system itself. A plausible explanation is that beta-emitting radioactive isotopes in FR-4-based PCB materials are the primary contributors to this background [39]. Both the anode readout board and field cage of the TPC were made of this type of material.

To examine this hypothesis, the TPC field cage was replaced with a low-background flexible PCB material, while keeping the rest of the system unchanged for comparison (see Fig. 14). This optimized PCB material has been successfully used to manufacture low-background Micromegas detectors for the PandaX-III experiment [40]. Its radioactive background was tested at the China JinPing Underground Laboratory (CJPL), demonstrating an extremely

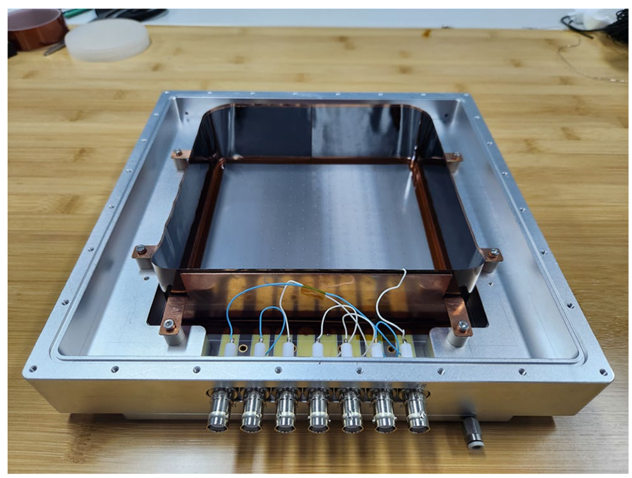

**Fig. 14** (Color online) A photograph of the TPC with a flexible PCB field cage

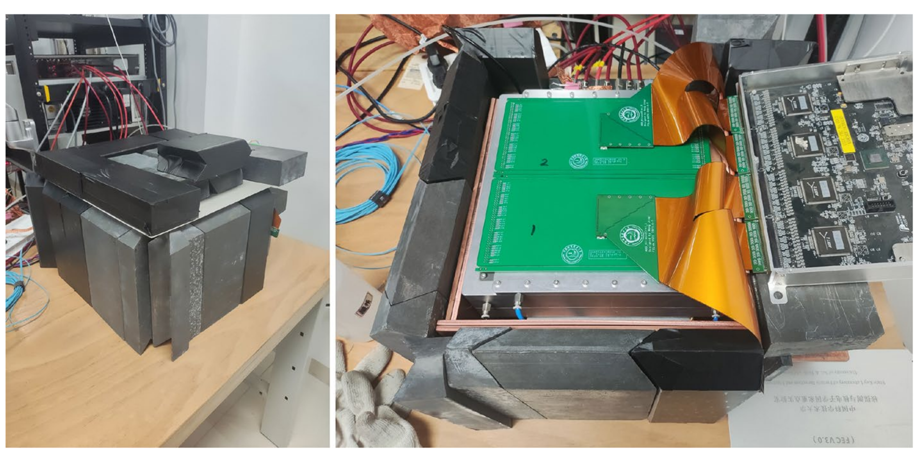

**Fig. 13** (Color online) Experimental setup for lead shielding test

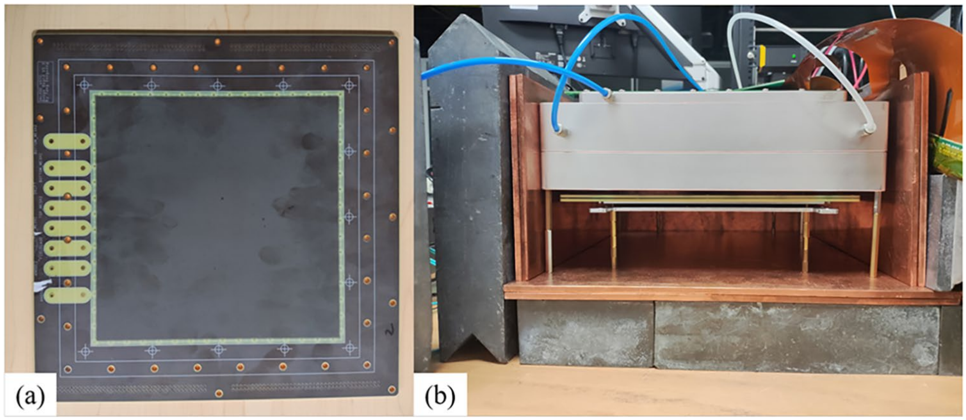


**Fig. 15** (Color online) (a) Anode PCB of the TPC system; (b) experimental setup for the anode PCB background test, where the anode PCB is positioned on an aluminum support structure close to the detector

**Table 1** Background count rates for different field cage materials with and without lead shielding

| Condition | Acquisition time (min) | Event number after cuts | Count rate (cpm/cm$^2$) |
|---|---|---|---|
| FR-4 PCB, not shielded | 120 | 16126 | 3.49 |
| FR-4 PCB, shielded | 120 | 4859 | 1.05 |
| Flexible PCB, not shielded | 240 | 27259 | 2.95 |
| Flexible PCB, shielded | 240 | 5982 | 0.65 |

**Table 2** Estimated background rates and their relative contributions to the total background for the original TPC design with an FR-4-based field cage

| Background component | Count rate (cpm/cm$^2$) | Fraction |
|---|---|---|
| Environmental gamma | 2.43 | 69.6% |
| Field cage | 0.40 | 11.5% |
| Anode board | 0.66 | 18.9% |
| Sum | 3.49 | 100% |

low-background level of 24 µBq/cm$^2$ [41, 42]. Therefore, implementing this low-radioactivity field cage is expected to reduce the background contribution to a negligible level. The TPC system with the new field cage was tested under the same conditions as the original system with and without shielding. The background event rates for different TPC configurations and experimental setups are summarized in Table 1. When the field cage material was replaced with the flexible PCB, the background count rate was reduced by 15.5% in the non-shielded setup and by 38.4% in the shielded setup. This indicates that the original FR-4 PCB field cage contributed approximately 11.6% to the total background in the non-shielded configuration, corresponding to approximately 0.40 cpm/cm$^2$.

To further estimate the background contribution from the anode PCB, an indirect test procedure was performed. In this test, the TPC system was shielded, and an identical anode PCB was placed under the TPC entrance window (see Fig. 15). The difference in background contribution was measured by comparing the background count rate in this setup with the rate without the additional PCB. An increase in the count rate was expected because beta particles emitted from the additional anode board could penetrate the entrance window and be detected. The results showed an increase of 7.4 cpm with the anode PCB in place. Although this measured count rate does not directly represent the actual contribution of the TPC anode PCB owing to the asymmetric layout of the two boards, it can be scaled using a conversion factor. This factor was derived by comparing the simulation results for both test setups. The input for the simulation, including beta-emitting isotopes and their activities, was obtained from Zhang et al. [39]. Using a simulated conversion factor of 3.45, the background contribution from the TPC anode PCB was estimated to be 0.66 cpm/cm$^2$. This value closely matches the remaining background of 0.65 cpm/cm$^2$ after shielding and replacing the field cage material, indicating that the anode PCB is another significant contributor to the beta background. To summarize, the estimated contributions of the three primary background components, along with their respective count rates and proportions, are listed in Table 2. Although other minor background sources may exist, such as radioactivity from additional detector materials or cosmic rays not vetoed by the anti-coincidence detector, their contributions to the total background are considered negligible.

## 7 Detector optimization and expected performance

The results in Table 2 show that environmental gamma radiation accounts for approximately 70% of the total background, while the remaining 30% originates from the

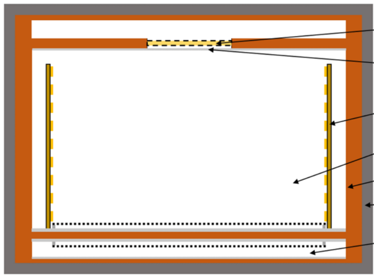


**Fig. 16** (Color online) Schematic of the optimized version of the TPC system

**Table 3** Simulated background rates for the optimized TPC system. The last column corresponds to the value after the TMVA BDT classification at 55% signal efficiency

| Lead thickness | Count rate before classification ($cpm/cm^2$) | Count rate after classification ($cpm/cm^2$) |
|---|---|---|
| 0.5 cm | 0.090 | 0.015 |
| 1 cm | 0.035 | 0.0058 |
| 2 cm | 0.008 | 0.0012 |

intrinsic beta radioactivity of the PCB. It is anticipated that the PCB-induced background can be significantly reduced by replacing the FR-4 material with a low-radioactivity flexible PCB material, as demonstrated by the substantial reduction in the background observed when the field cage was replaced, as described in Sect. 6. Therefore, the critical factor in achieving an even lower background rate is reducing the environmental gamma-induced background, which remains the dominant source of beta radiation. To achieve this, a new version of the TPC with an optimized detector layout was designed to strike a balance between mitigating the background and maintaining detector portability. A schematic representation of the optimized TPC is shown in Fig. 16. In addition to utilizing low-background PCB materials, the entire mechanical structure was replaced with oxygen-free copper. This material has a higher atomic number ($Z$) than aluminum and features a lower intrinsic radiation level than standard copper types [43]. To further reduce the background contributions from the surrounding environment, additional shielding layers were incorporated around the TPC system. The shielding consists of an outer layer of lead with a thickness ranging from 0.5 cm to 2 cm, and a 0.5 cm thick inner layer of oxygen-free copper, which serves to block any intrinsic beta decay from the lead itself.

Simulations were conducted to evaluate the expected performance of the new TPC design, focusing on the environmental gamma background, as the contribution from the flexible PCB material was eliminated. The simulation considered three different lead shielding thicknesses, and the results are summarized in Table 3. The results indicate that with a lead shielding thickness of 2 cm, the environmental gamma background is reduced to 0.33% of the current level without BDT classification. With a beta signal efficiency of 55%, the remaining background was further reduced to 0.05%. This leads to an exceptionally low background rate of 0.0012 $cpm/cm^2$ in a 7 cm diameter region.

## 8 Conclusion

In this study, a TPC prototype for beta radiation detection was designed and fabricated. The TPC is equipped with a micromegas detector to eliminate the cosmic ray background through anti-coincidence. The test results demonstrated that the TPC system can reconstruct beta particle tracks and energy depositions. A simulation program was developed to assess the performance of the TPC system, including a digitization process to convert the simulation results into the signal waveforms. The simulated data aligned well with the test data according to the distribution of various variables. Several multivariate analysis models were evaluated to discriminate between beta and background data, with the TMVA BDT model selected for its superior performance. The BDT method, which was trained using the simulation datasets, was then applied to classify the test data. With this discrimination method, the TPC system achieved a background rate of 0.49 $cpm/cm^2$ without shielding, while retaining 55% of the beta events. The source of the beta background was investigated by comparing the results obtained using different detector settings. Environmental gamma radiation, anode board radioactivity, and field cage radioactivity are the three primary contributors to the beta background.

An optimized version of the detector, featuring a low-background flexible PCB material and oxygen-free copper, was designed to further minimize the background noise. The simulation results indicated that this new TPC design is expected to achieve a total background rate of 0.0012 $cpm/cm^2$ with a beta signal efficiency of 55%. The new version of the TPC holds promise for practical applications.

**Acknowledgements** This work was partially performed at the University of Science and Technology of China (USTC) Center for Micro and Nanoscale Research and Fabrication, and we thank Yu Wei for his help with the nanofabrication steps of the germanium coating for the resistive anodes. For the development of the TPC prototype, we are grateful to Dr. Sicheng Wen, Dr. Anshun Zhou, and the R&D team of JIANWEI Scientific Instruments Technology Co., Ltd.

**Author contributions** All authors contributed to the study conception and design. Material preparation, data collection and analysis were performed by Rui-Yang Zhang. The first draft of the manuscript was written by Rui-Yang Zhang and all authors commented on previous versions of the manuscript. All authors read and approved the final manuscript.

**Data availability** The data that support the findings of this study are openly available in Science Data Bank at https://cstr.cn/31253.11.sciencedb.j00186.00939 and https://doi.org/10.57760/sciencedb.j00186.00939.

## Declarations

**Conflict of interest** The authors declare that they have no conflict of interest.

## References

1. E. Rutherford, VIII. Uranium radiation and the electrical conduction produced by it. London Edinburgh Philos. Mag. J. Sci. **47**(284), 109–163 (1899). https://doi.org/10.1080/14786449908621245
2. D. Shahbazi-Gahrouei, M. Gholami, S. Setayandeh et al., A review on natural background radiation. Adv. Biomed. Res. **2**(1), 65 (2013). https://doi.org/10.4103/2277-9175.115821
3. S. Li, H.P. Wang, Y.X. Zhang, Assessment of supervision monitoring for radiation environment around the typical research reactors in China. Nucl. Eng. Technol. **53**(12), 4150–4157 (2021). https://doi.org/10.1016/j.net.2021.06.032
4. T. Kubota, Y. Shibahara, S. Fukutani et al., Cherenkov counting of $^{90}$Sr and $^{90}$Y in bark and leaf samples collected around Fukushima Daiichi Nuclear Power Plant. J. Radioanal. Nucl. Ch. **303**(1), 39–46 (2015). https://doi.org/10.1007/s10967-014-3348-y
5. Y. Gao, Y.L. Zhu, Analysis of the influence on environmental radiation level of Qinshan area caused by Fukushima nuclear accident. Nucl. Sci. Tech. **25**(1), S010606 (2014). https://doi.org/10.13538/j.1001-8042/nst.25.S010606
6. Y. Cao, J. Lin, K. Zhai et al., Long-term investigation of environmental radioactivity levels and public health around the Qinshan Nuclear Power Plant. China. Sci. Rep. **12**, 4945 (2022). https://doi.org/10.1038/s41598-022-09091-2
7. J.A. Formaggio, C.J. Martoff, Backgrounds to sensitive experiments underground. Annu. Rev. Nucl. Part. S. **54**, 361–412 (2004). https://doi.org/10.1146/annurev.nucl.54.070103.181248
8. E. Aprile, K. Arisaka, F. Arneodo et al., Study of the electromagnetic background in the XENON100 experiment. Phys. Rev. D **83**(8), 082001 (2011). https://doi.org/10.1103/PhysRevD.83.082001
9. P. Novella, B. Palmeiro, M. Sorel et al., Radiogenic backgrounds in the NEXT double beta decay experiment. J. High Energy Phys. **2019**, 051 (2019). https://doi.org/10.1007/JHEP10(2019)051
10. X.G. Cao, Y.L. Chang, K. Chen et al., NνDEx-100 conceptual design report. Nucl. Sci. Tech. **35**, 3 (2024). https://doi.org/10.1007/s41365-023-01360-7
11. X.X. Miao, Y.Q. Ji, X.Z. Shao et al., Radioactivity of drinking-water in the vicinity of nuclear power plants in China based on a large-scale monitoring study. Int. J. Env. Res. Pub. He. **10**, 6863–6872 (2013). https://doi.org/10.3390/ijerph10126863
12. C. Sang, W. An, P.B. Sorensen et al., Gross alpha and beta measurements in drinkable water from seven major geographical regions of China and the associated cancer risks. Ecotoxicol. Environ. Saf. **208**, 111728 (2021). https://doi.org/10.1016/j.ecoenv.2020.111728
13. L. Zhou, R. Wang, H. Ren et al., Detection of polonium-210 in environmental, biological and food samples: a review. Molecules **28**, 6268 (2023). https://doi.org/10.3390/molecules28176268
14. Y. Cao, Z. Zhao, H. Zou et al., Radioactivity in water and food from Hangzhou, China in the past decade: levels, sources, exposure and human health risk assessment. Environ. Technol. Innov. **28**, 102581 (2022). https://doi.org/10.1016/j.eti.2022.102581
15. B. Yang, Q. Zhou, J. Zhang et al., Evaluation of the natural radioactivity in food and soil around uranium mining region. J. Radioanal. Nucl. Ch. **329**, 127–133 (2021). https://doi.org/10.1007/s10967-021-07794-w
16. F.J. Walter, R.R. Boshart, Low background counting of betas and alphas with silicon detectors. Nucl. Instrum. Meth. **42**(1), 1–14 (1966). https://doi.org/10.1016/0029-554X(66)90261-8
17. G. Heusser, Low-radioactivity background techniques. Annu. Rev. Nucl. Part. S. **45**, 543–590 (1995). https://doi.org/10.1146/annurev.ns.45.120195.002551
18. V. Jobbagy, U. Waetjen, J. Meresova, Current status of gross alpha/beta activity analysis in water samples: a short overview of methods. J. Radioanal. Nucl. Ch. **286**, 393–399 (2010). https://doi.org/10.1007/s10967-010-0709-z
19. W.K. Warburton, B. Dwyer-McNally, Electronic background rejection in a new ultra-low background alpha-particle counter. Nucl. Instrum. Meth. B **263**, 221–224 (2007). https://doi.org/10.1016/j.nimb.2007.04.089
20. ORTEC: MPC-9604 Alpha/Beta Counting Multi-Detector System (2025), https://www.ortec-online.com/products/systems/gross-alpha-beta-measurement-systems/alpha-beta-counting-systems/mds/. Accessed 6 Jan 2025
21. Z.H. Zhang, Y.F. Zhang, C.Y. Hu et al., Detection and discrimination of $\alpha$- and $\beta$-radiation with plastic scintillators based on pulse shape discrimination. J. Instrum. **15**, P04008 (2020). https://doi.org/10.1088/1748-0221/15/04/P04008
22. Z. Shao, Z. Wang, J. Liu et al., Design of a portable phoswich detector for simultaneous $\alpha$, $\beta$, and $\gamma$ identification. IEEE Trans. Nucl. Sci. **69**, 2281–2289 (2022). https://doi.org/10.1109/TNS.2022.3218818
23. J. Pan, Z.Y. Zhang, C.Q. Feng et al., An ultra-low background alpha detection system with a Micromegas-based time projection chamber. Rev. Sci. Instrum. **93**, 013303 (2022). https://doi.org/10.1063/5.0070612
24. H.Y. Du, C.B. Du, K. Giboni et al., Screener3D: a gaseous time projection chamber for ultra-low radioactive material screening. Nucl. Sci. Tech. **32**, 142 (2021). https://doi.org/10.1007/s41365-021-00983-y
25. H. Du, C. Du, K. Han et al., A gaseous time projection chamber with Micromegas readout for low-radioactive material screening. Radiat. Detect. Technol. Methods **7**, 90–99 (2023). https://doi.org/10.1007/s41605-022-00364-y
26. K. Siegbahn, *Alpha-, Beta- and Gamma-Ray Spectroscopy* (Elsevier Science, 2012)
27. J.X. Feng, Z.Y. Zhang, J.B. Liu et al., A thermal bonding method for manufacturing Micromegas detectors. Nucl. Instrum. Meth. A **989**, 164958 (2021). https://doi.org/10.1016/j.nima.2020.164958
28. Z. Zhang, F. Wang, Z. Yang et al., Manufacture and performance of the thermal-bonding Micromegas prototype. J. Instrum. **9**, C10028 (2014). https://doi.org/10.1088/1748-0221/9/10/C10028
29. J.X. Feng, Z.Y. Zhang, J.B. Liu et al., A novel resistive anode using a germanium film for Micromegas detectors. Nucl. Instrum. Meth. A **1031**, 166595 (2022). https://doi.org/10.1016/j.nima.2022.166595
30. T. Behnke, K. Dehmelt, R. Diener et al., A lightweight field cage for a large TPC prototype for the ILC. J. Instrum. **5**, P10011 (2010). https://doi.org/10.1088/1748-0221/5/10/P10011

31. S. Anvar, P. Baron, B. Blank et al., AGET, the GET front-end ASIC, for the readout of the Time Projection Chambers used in nuclear physic experiments. Paper Presented at 2011 IEEE Nuclear Science Symposium Conference Record (Valencia, Spain, 2011). https://doi.org/10.1109/NSSMIC.2011.6154095
32. D.Y. Zhu, S.B. Liu, C.Q. Feng et al., Development of the front-end electronics for PandaX-III prototype TPC. IEEE Trans. Nucl. Sci. **66**(7), 1123–1129 (2019). https://doi.org/10.1109/TNS.2019.2907125
33. NuDat3.0: Search and plot nuclear structure and decay data interactively (2025), https://www.nndc.bnl.gov/nudat3/. Accessed 6 Jan 2025
34. S. Agostinelli, J. Allison, K. Amako et al., GEANT4 - a simulation toolkit. Nucl. Instrum. Meth. A **506**, 250–303 (2003). https://doi.org/10.1016/S0168-9002(03)01368-8
35. Garfield++ (2025), https://garfieldpp.web.cern.ch/garfieldpp/. Accessed 6 Jan 2025
36. T.Y. Liu, M.X. Xue, H.P. Peng et al., Unfolding environmental $\gamma$ flux spectrum with portable CZT detector. Nucl. Instrum. Meth. A **1063**, 169315 (2024). https://doi.org/10.1016/j.nima.2024.169315
37. C.C. Aggarwal, *in Data Mining: The Textbook* (Springer International Publishing, 2015), pp.285–344
38. A. Hoecker, P. Speckmayer, J. Stelzer et al., TMVA - Toolkit for multivariate data analysis (2007). arXiv:physics/0703039
39. X. Zhang, S. Niu, Y. Xie et al., Study of new substrate THGEMs with low neutron scattering and low radioactivity. J. Instrum. **10**, P10043 (2015). https://doi.org/10.1088/1748-0221/10/10/P10043
40. X. Chen, C.B. Fu, J. Galan et al., PandaX-III: Searching for neutrinoless double beta decay with high pressure $^{136}$Xe gas time projection chambers. Sci. China Phys. Mech. **60**(6), 061011 (2017). https://doi.org/10.1007/s11433-017-9028-0
41. S.C. Wen, Z.Y. Zhang, Y.Z. Peng et al., Design and fabrication of low background, high energy resolution thermal bonding Micromegas detectors for the PandaX-III experiment. Nucl. Instrum. Meth. A **1062**, 169206 (2024). https://doi.org/10.1016/j.nima.2024.169206
42. Y.K. Yao, T. Zhang, C. Cheng et al., Sensitivity analysis of gamma spectroscopy system with dual high-purity germanium detectors. Nucl. Tech. (in Chinese) **45**(08), 080403 (2022). https://doi.org/10.11889/j.0253-3219.2022.hjs.45.080403
43. E.W. Hoppe, C.E. Aalseth, O.T. Farmer et al., Reduction of radioactive backgrounds in electroformed copper for ultra-sensitive radiation detectors. Nucl. Instrum. Meth. A **764**, 116–121 (2014). https://doi.org/10.1016/j.nima.2014.06.082